Quantitative agreement between electron-optical phase images of WSe_2 and simulations based on electrostatic potentials that include bonding effects

S. Borghardt,[1] F. Winkler,[2,3] Z. Zanolli,[4,5,7] M. J. Verstraete,[6,7]
J. Barthel,[2,8] A. H. Tavabi,[2,3] R. E. Dunin-Borkowski,[2,3] and B. Kardynal[1]

[1]*Peter Grünberg Institute 9 (PGI-9), Forschungszentrum Jülich, D-52425 Jülich, Germany*
[2]*Ernst Ruska-Centre for Microscopy and Spectroscopy with Electrons (ER-C), Forschungszentrum Jülich, D-52425 Jülich, Germany*
[3]*Peter Grünberg Institute 5 (PGI-5), Forschungszentrum Jülich, D-52425 Jülich, Germany*
[4]*Peter Grünberg Institute 1 (PGI-1) and Institute for Advanced Simulations (IAS-1), Forschungszentrum Jülich, D-52425 Jülich, Germany*
[5]*Institute for Theoretical Solid State Physics, RWTH Aachen University, D-52056 Aachen, Germany*
[6]*Physique des matériaux et nanostructures (NanoMat), CESAM and Département de Physique, Université de Liège (B5), B-4000 Liège, Belgium*
[7]*European Theoretical Spectroscopy Facility, http://www.etsf.eu*
[8]*Gemeinschaftslabor für Elektronenmikroskopie (GFE), RWTH Aachen University, D-52074 Aachen, Germany*

DETAILED DESCRIPTION OF THE ELECTROSTATIC POTENTIAL CALCULATIONS

The pseudopotential calculations in this work were performed using the ABINIT software package [1, 2] with the Perdew-Zunger-Ceperley-Alder LDA exchange-correlation functional [3] and optimized norm-conserving Vanderbilt pseudopotentials, following the scheme of Hamann [4]. Convergence studies were used to choose a plane wave cutoff energy of 32 Ha and an 8×8×1 Monkhorst-Pack k-point grid [5], thereby ensuring convergence of the system's total energy below 0.1%. In order to avoid interactions between periodic images of the finite thickness slab, a vacuum layer with a thickness of 22 Å was included in the supercell between the outermost Se planes of two neighbouring periodic images of the slab.

For the relaxation calculations, tolerances on the maximal force and stress in the relaxation calculations were set to $5 \cdot 10^{-5} \frac{\mathrm{Ha}}{a_0}$ and $5 \cdot 10^{-7} \frac{\mathrm{Ha}}{a_0^3}$, respectively.

For calculations of electrostatic potentials, the spatial resolution of the DFT calculation was improved by increasing the plane wave cutoff energy to 48 Ha. The high spatial resolution was necessary for the treatment of sharp electrostatic potentials in the core regions.

Electrostatic potentials were calculated using a combination of pseudopotential and all-electron DFT calculations [6] (Fig. 1). For each element of interest (Se and W), isolated atom Γ-point all-electron calculations in a cubic supercell with a side length of 10.5 Å were performed using the Elk code with its default computation parameters. The resulting electrostatic potentials were compared with individual atom pseudopotential calculations performed

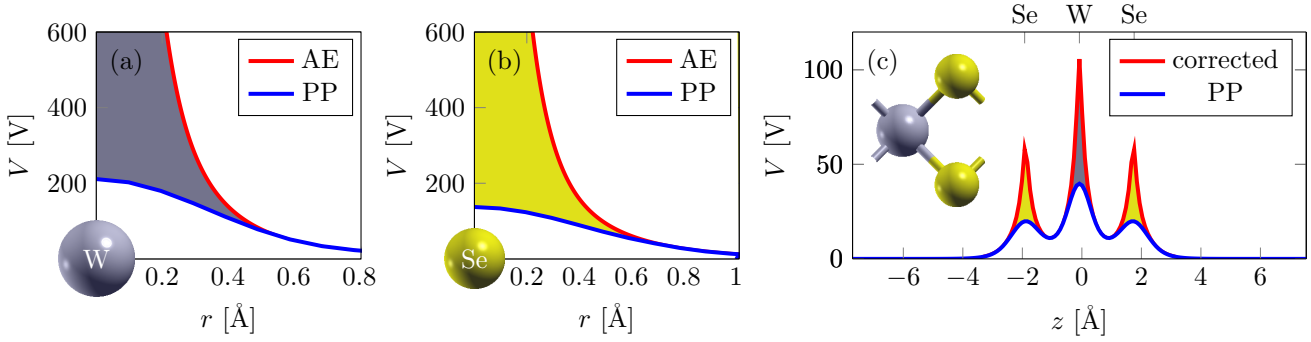

FIG. 1: Combination of all electron and pseudopotential DFT methods for the calculation of electrostatic potentials. First, single atom calculations were performed for each element of interest using both methods. (a) and (b) show the electrostatic potentials of W and Se atoms, respectively, as a function of distance from the nucleus position. The differences (colored areas between the curves) were used as a correction term in the calculation of the electrostatic potential of the system of interest. For the WSe_2 monolayer structure, (c) shows both the electrostatic potential determined from the pseudopotential calculation and corrected electrostatic potential. Here, the plane average of the electrostatic potential is shown.

under identical conditions. The difference, which results from the modified core potentials in the pseudopotential method, was saved for further use. The complete crystal unit cells were then treated using pseudopotential calculations and the precalculated difference terms were added in order to obtain full DFT electrostatic potentials for subsequent off-axis electron holography simulations.

In addition to the DFT electrostatic potentials, independent DFT (IDFT) electrostatic potentials were calculated. In this method, isolated atom pseudopotential calculations were performed for individual atoms and their electrostatic potentials were then superimposed to obtain crystal potentials. These potentials were also corrected using the all electron terms, as described for the DFT method.

COMPARISON BETWEEN SIMULATIONS AND EXPERIMENTAL RESULTS

Figure 2 shows the experimental phase image, to which the results of the simulations were compared. Table I lists the parameters that were used for the correction of aberrations in the experimental data. Table II lists the parameters that were used for the multislice simulations. Table III shows the agreement obtained between the simulations and experimental data for the WSe_2 bilayer structure. Figure 3 shows the difference between phase images of a WSe_2 bilayer calculated using the DFT and IDFT methods. An estimate of the noise level required to measure bonding effects experimentally can be obtained from this figure.

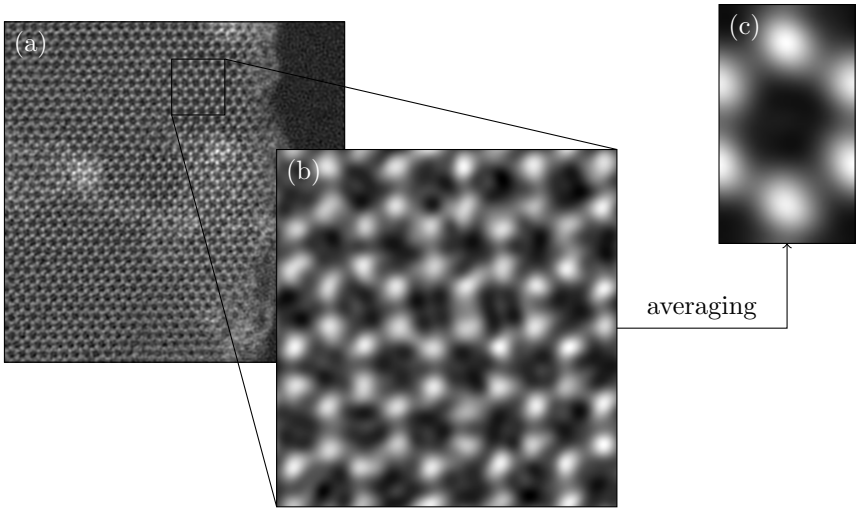

FIG. 2: Aberration corrected experimental phase image of a WSe_2 bilayer. (a) shows the full experimental phase image of the electron wave function presented in [7]. (b) shows a magnified view of an area that appears to be clean and almost free of defects. This area has a size of 5x3 orthorhombic unit cells. (c) shows a cell-averaged phase image of the area shown in (b).

$A_1 =$	1.08nm	$(-115°)$	$C_1 =$	-3.68nm	
$A_2 =$	174nm	$(-134°)$	$B_2 =$	135nm	$(-96°)$
$A_3 =$	2.29μm	$(-168°)$	$S_3 =$	2.84μm	$(-135°)$
$C_3 =$	13.6μm		$C_5 =$	-6.5μm	

TABLE I: Residual coherent aberration coefficients used to correct the experimental image wave function of the WSe_2 bilayer (Fig. 2). The parameters were obtained by means of a Nelder-Mead minimization [8] of the root mean square differences between experimental and simulated real-space phase maps of the respective image wave functions for an average projected orthorhombic unit cell (Fig. 2 (c)).

	Monolayer	Bilayer
Electron energy	$E = 80$ keV	$E = 80$ keV
Aperture	$\alpha = 15$ mrad	$\alpha = 42$ mrad
Debye-Waller parameters	$B_{Se} = B_W = 0.3$ Å^2	$B_{Se} = B_W = 0.3$ Å^2
Specimen tilt	$t_x = t_y = 0^\circ$	$t_x = -2.74^\circ$, $t_y = 0.41^\circ$
Image wave convolution	$s_1 = s_2 = 22$ pm	$s_1 = 43$ pm, $s_2 = 32$ pm, $s_1 \sphericalangle x = -56^\circ$

TABLE II: Simulation parameters for the multislice simulations of electron-optical phase images for WSe_2 monolayer and bilayer structures. Debye-Waller parameters were taken from the literature [9]. In the case of monolayer WSe_2 the simulation was performed for an untilted sample and the other parameters represent typical experimental values. In the case of bilayer WSe_2, the parameters for sample tilt and quasi-coherent image wave convolution were obtained by means of a Nelder-Mead minimization [8] of the root mean square differences between the 13 strongest experimental and simulated beam amplitudes in the Fourier transforms of the respective image wave functions.

	Minimum Diff. [mrad]	Mean Diff. [mrad]	Maximum Diff. [mrad]	RMS Diff. [mrad]
IAA	−61	−25	18	28
IDFT	−52	−16	29	21
DFT	−36	−3	38	13

TABLE III: Agreement between the spatially-resolved experimental and simulated electron phases. The table shows the minimum, mean and maximum difference in electron phase, as well as the root mean square of the difference, for the three different simulation methods used in this work.

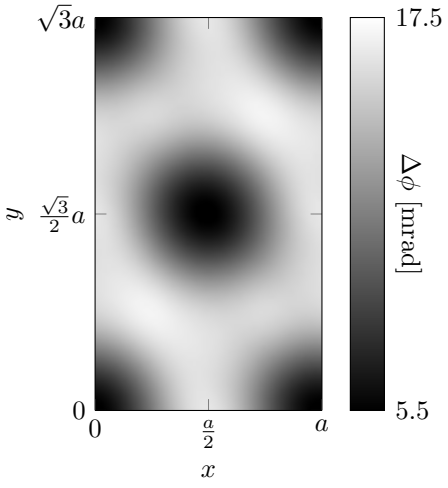

FIG. 3: Difference between the electron phase calculated for a WSe_2 bilayer using the DFT and IDFT methods. The area shown corresponds to the area marked by a blue rectangle in Fig. 1 in the main text. Positive values correspond to a larger electron phase in the IDFT method. The largest difference in electron phase can be found along the bonding directions of the WSe_2 crystal, whereas only small differences are found in the interstitial areas. The standard deviation of the difference image is 3 mrad.

[1] X. Gonze *et al.*, Comput. Phys. Commun. **180**, 2582-2615 (2009).
[2] X. Gonze *et al.*, Z. Kristallogr. **220**, 558-562 (2005).
[3] J.P. Perdew and A. Zunger, Phys. Rev. B **23**, 5048-5079 (1981).
[4] D.R. Hamann, Phys. Rev. B **88**, 085117 (2013).
[5] H. J. Monkhorst and J. D. Pack, Phys. Rev. B **13**, 5188 (1976).
[6] W.L. Wang and E. Kaxiras, Phys. Rev. B **87**, 085103 (2013).
[7] F. Winkler, A.H. Tavabi, J. Barthel, M. Duchamp, E. Yucelen, S. Borghardt, B.E. Kardynal, R.E. Dunin-Borkowski, Ultramicroscopy (2016), in press. doi: 10.1016/j.ultramic.2016.07.016.
[8] J.A. Nelder and R. Mead, The Computer Journal **7**, 308-313 (1965).
[9] F.Z. Chien, Y.S. Chen, Y.C. Chu, W.Y. You, J.B. Lee, T.E. Dann, C.H. Tu and Y.S. Huang, Chinese Journal of Physics **26**, 119 (1988).